

Exploring dopant-enhanced ionic conductivity of AgCl-doped $\text{Li}_7\text{P}_3\text{S}_{11}$ solid electrolytes

Choi, Yong-Seok; Lee, Youngin; Ahn, Hyuna; Jeong, Jiwon; Chung, Kyung Yoon; Scanlon, David O.; Lee, Jae-Chul

DOI:

[10.1002/cey2.564](https://doi.org/10.1002/cey2.564)

License:

Creative Commons: Attribution (CC BY)

Document Version

Publisher's PDF, also known as Version of record

Citation for published version (Harvard):

Choi, YS, Lee, Y, Ahn, H, Jeong, J, Chung, KY, Scanlon, DO & Lee, JC 2024, 'Exploring dopant-enhanced ionic conductivity of AgCl-doped $\text{Li}_7\text{P}_3\text{S}_{11}$ solid electrolytes: Integrating synchrotron Rietveld analysis, DFT, and ANN-based molecular dynamics approaches', *Carbon Energy*. <https://doi.org/10.1002/cey2.564>

[Link to publication on Research at Birmingham portal](#)

General rights

Unless a licence is specified above, all rights (including copyright and moral rights) in this document are retained by the authors and/or the copyright holders. The express permission of the copyright holder must be obtained for any use of this material other than for purposes permitted by law.

- Users may freely distribute the URL that is used to identify this publication.
- Users may download and/or print one copy of the publication from the University of Birmingham research portal for the purpose of private study or non-commercial research.
- User may use extracts from the document in line with the concept of 'fair dealing' under the Copyright, Designs and Patents Act 1988 (?)
- Users may not further distribute the material nor use it for the purposes of commercial gain.

Where a licence is displayed above, please note the terms and conditions of the licence govern your use of this document.



When citing, please reference the published version.

Take down policy

While the University of Birmingham exercises care and attention in making items available there are rare occasions when an item has been uploaded in error or has been deemed to be commercially or otherwise sensitive.

If you believe that this is the case for this document, please contact UBIRA@lists.bham.ac.uk providing details and we will remove access to the work immediately and investigate.

Exploring dopant-enhanced ionic conductivity of AgCl-doped $\text{Li}_7\text{P}_3\text{S}_{11}$ solid electrolytes: Integrating synchrotron Rietveld analysis, DFT, and ANN-based molecular dynamics approaches

Yong-Seok Choi¹ | Youngin Lee² | Hyuna Ahn² | Jiwon Jeong^{2,3} |
Kyung Yoon Chung³  | David O. Scanlon⁴ | Jae-Chul Lee^{2,5} 

¹Department of Materials Science and Engineering, Dankook University, Cheonan, South Korea

²Department of Materials Science and Engineering, Korea University, Seoul, South Korea

³Center for Energy Storage Research, Korea Institute of Science and Technology, Seoul, South Korea

⁴The School of Chemistry, University of Birmingham, Edgbaston, Birmingham, UK

⁵Institute of Green Manufacturing Research, Korea University, Seoul, South Korea

Correspondence

Jae-Chul Lee, Department of Materials Science and Engineering, Korea University, Seoul 02841, South Korea.
Email: jclee001@korea.ac.kr

Funding information

National Research Foundation of Korea, Grant/Award Numbers: MEST, NRF-2021R1A2C2009596; Engineering and Physical Sciences Research Council, Grant/Award Numbers: EP/R029431, EP/P020194, EP/T022213; Korea government (Ministry of Science and ICT, MSIT), Grant/Award Number: RS-2023-00236572; European Research Council, ERC, Grant/Award Numbers: EP/R029431, EP/P020194, EP/T022213

Abstract

The effectiveness of dual-doping as a method of improving the conductivity of sulfide solid electrolytes (SEs) is not in doubt; however, the atomic-level mechanisms underpinning these enhancements remain elusive. In this study, we investigate the atomic mechanisms associated with the high ionic conductivity of the $\text{Li}_7\text{P}_3\text{S}_{11}$ (LPS) SE and its response to Ag/Cl dual dopants. Synthesis and electrochemical characterizations show that the 0.2 M AgCl-doped LPS ($\text{Li}_{6.8}\text{P}_3\text{Ag}_{0.1}\text{S}_{10.9}\text{Cl}_{0.1}$) exhibited an over 80% improvement in ionic conductivity compared with the undoped LPS. The atomic-level structures responsible for the enhanced conductivity were generated by a set of experiment and simulation techniques: synchrotron X-ray diffractometry, Rietveld refinement, density functional theory, and artificial neural network-based molecular dynamics simulations. This thorough characterization highlights the role of dual dopants in altering the structure and ionic conductivity. We found that the PS_4 and P_2S_7 structural motifs of LPS undergo transformation into various PS_x substructures. These changes in the substructures, in conjunction with the paddle-wheel effect, enable rapid Li migration. The dopant atoms serve to enhance the flexibility of PS_4 - P_2S_7 polyhedral frameworks, consequently enhancing the ionic conductivity. Our study elucidates a clear structure–conductivity relationship for the dual-doped LPS, providing a fundamental guideline for the development of sulfide SEs with superior conductivity.

KEYWORDS

density functional theory, molecular dynamics, paddle-wheel dynamics, sulfide solid electrolytes, synchrotron Rietveld analysis

Yong-Seok Choi, Youngin Lee, and Hyuna Ahn contributed equally to this study.

This is an open access article under the terms of the [Creative Commons Attribution](https://creativecommons.org/licenses/by/4.0/) License, which permits use, distribution and reproduction in any medium, provided the original work is properly cited.

© 2024 The Authors. *Carbon Energy* published by Wenzhou University and John Wiley & Sons Australia, Ltd.

1 | INTRODUCTION

Dual doping with metal halides (MX; M = metals, X = F, Cl, Br, or I) has proven to be a straightforward strategy to achieve high-conductivity sulfide solid electrolytes (SEs).^{1–4} The inception of this technique can be traced back to the work of Kato et al.,⁵ in which the authors added Si and Cl dopants to replace the host atoms comprising the $x\text{Li}_2\text{S}-y\text{P}_2\text{S}_5$ electrolytes. Since then, extensive studies on dual-doping with various dopants, such as MnI,⁶ CuCl,⁷ AgI,⁸ and W with Br dopants⁹ were reported. Although superionic conductivities of $>10^{-3}\text{ S cm}^{-1}$ could be obtained with this method, the underlying reasons for such improvements remained mostly qualitative. Preliminary investigations identified the presence of several substructures, such as PS_4 , P_2S_6 , and P_2S_7 , within SEs based on $x\text{Li}_2\text{S}-y\text{P}_2\text{S}_5$ compositions.^{1,10–12} Subsequent studies examined the roles of these substructures to elucidate the structure–conductivity relationship in dual-doped SEs. However, owing to the difficulty in generating the atomic-scale structures representing the electrolytes and the severe spatiotemporal limitations of the employed simulations, previous studies were not successful in specifying the substructures responsible for the observed conductivity.^{8,13,14} As a result, the roles of dual dopants in enhancing conductivity are yet to be established.

All undoped SEs with $x\text{Li}_2\text{S}-y\text{P}_2\text{S}_5$ compositions are composed of various phases/crystals, such as Li_3PS_4 , $\text{Li}_7\text{P}_3\text{S}_{11}$, and $\text{Li}_4\text{P}_2\text{S}_6$, each of which is again constructed with the PS_4 , P_2S_6 , and P_2S_7 substructures (hereinafter, referred to as the “ PS_x ” motifs or ionic clusters without discrimination).^{15,16} Simulation studies showed that spaces surrounded by the vertices/corners (i.e., S atom sites) of these PS_x motifs construct the interpenetrating networks of diffusion channels, through which Li ions can migrate.¹⁷ The nature of these channels can vary depending on the chemical composition and synthesis method of the electrolytes because these process parameters can alter the spatial distribution and volume fractions of the PS_x motifs.¹⁰ The changes in the atomic-scale structures can restructure the diffusion channels and affect associated diffusion mechanisms, such as the so-called paddle-wheel effect^{18,19} and Li cooperative hopping,^{20,21} causing changes in the ionic conductivity of the dual-doped LPS.

For a comprehensive understanding of the effects of dopants on ionic conductivity, it is essential to work with reliable three-dimensional (3D) atomic structures and advanced analytical methods. While synchrotron X-ray diffractometry combined with Rietveld refinement can provide the required 3D atomic structures for SEs, traditional atomistic simulations, largely reliant on

density functional theory (DFT), have faced computational bottlenecks. The advent of artificial neural network-based molecular dynamics (ANN-based MD) presents a solution, offering the ability to manage large structures over extended time periods. By integrating experimental techniques like synchrotron X-ray diffractometry and Rietveld refinement and simulation techniques such as DFT and ANN-based MD, we can achieve a more thorough understanding of how dopants impact ionic conductivity. Furthermore, this integrated approach helps overcome the limitations of previous DFT-centric studies, which often focused on the partial effects of each diffusion mechanism. The enhanced accuracy and broader spatiotemporal scale of investigation achieved through this combined method enable more complete insights into the behavior of various substructures comprising electrolyte crystals, thus benefiting the development and optimization of SEs.

In this study, comparative studies were performed on the SEs with $70\text{Li}_2\text{S} - 30\text{P}_2\text{S}_5$ composition (hereinafter, referred to as “LPS”) and LPS added with up to 5.6 wt% (or 0.4 M) AgCl (hereinafter, referred to as “AgCl-doped LPS”) to explore the synergistic impact of the dual dopants in enhancing the ionic conductivity. Experiments demonstrated that the addition of 0.2 M AgCl to LPS led to a remarkable $>80\%$ increase in the ionic conductivity, reaching 2.39 mS cm^{-1} . To unravel the underlying mechanisms and achieve a more complete comprehension of diffusion processes, a range of techniques were employed, encompassing synchrotron X-ray diffractometry, Rietveld refinement, DFT calculations, and ANN-based MD simulations. Utilizing these advanced analytical approaches, we gained deeper insights into the role of dopant design in the enhancement of Li-ion transport within SEs.

2 | RESULTS AND DISCUSSION

2.1 | Synthesis and characterization of AgCl-doped LPS SEs

To investigate the effects of Ag and Cl doping on the ionic conductivity of LPS-type SEs, we synthesized LPS and AgCl-doped LPS with four different AgCl molar ratios (M) of 0.1, 0.2, 0.3, and 0.4 using the dry-milling method (see Methods in the Supporting Information), resulting in the samples with chemical formulae of $\text{Li}_{7-2x}\text{P}_3\text{Ag}_x\text{S}_{11-x}\text{Cl}_x$ with $x = 0.0, 0.05, 0.1, 0.15, \text{ and } 0.2$. The ionic conductivity of the samples was determined by measuring the impedance spectra (or Nyquist plots) using electrochemical impedance spectroscopy (Figure 1A). The measured Nyquist plots commonly consist of an incomplete

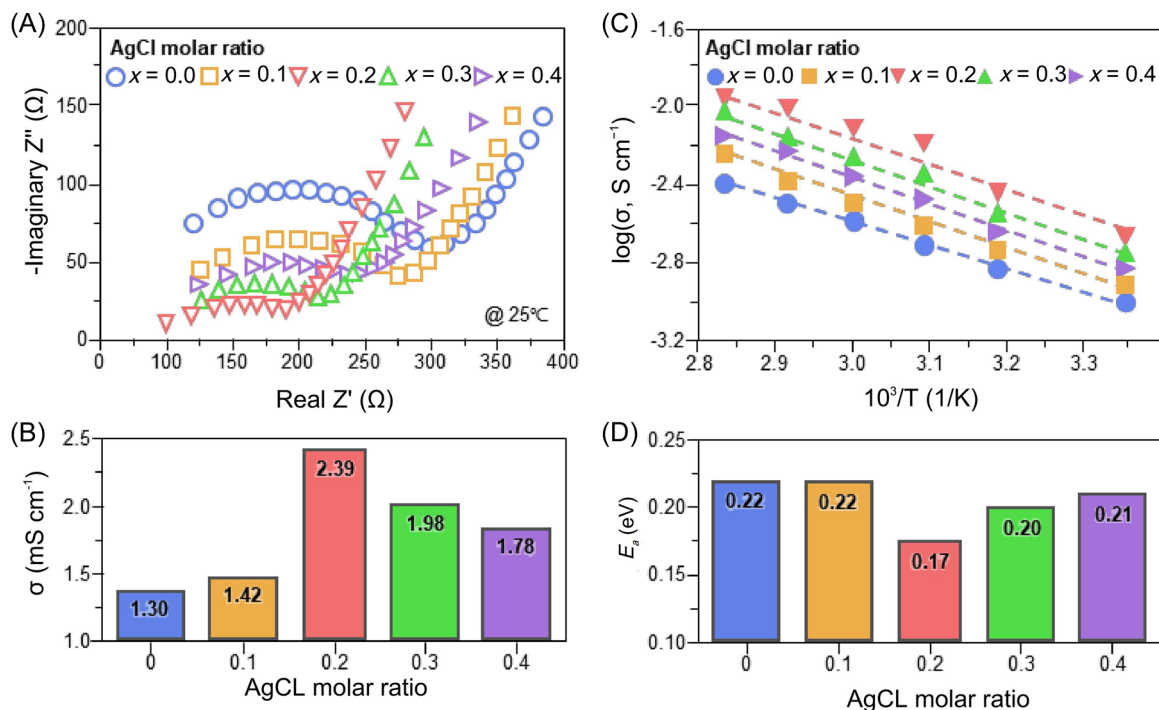


FIGURE 1 (A) Nyquist plots of the undoped LPS and AgCl-doped LPS with 0.1, 0.2, 0.3, and 0.4 molar ratios of AgCl (i.e., $\text{Li}_{7-2x}\text{P}_3\text{Ag}_x\text{S}_{11-x}\text{Cl}_x$ with $x = 0.0, 0.05, 0.1, 0.15, \text{ and } 0.2$) measured at 25°C. (B) Ionic conductivities measured from (A). (C) Arrhenius plots of the ionic conductivity of the undoped LPS and AgCl-doped LPS samples measured at varying temperatures of 25°C, 40°C, 50°C, 60°C, 70°C, and 80°C. (D) Energy barriers of the LPS and AgCl-doped LPS samples estimated from (C).

semicircle that includes the combined effects of the charge transfer resistance, grain boundary resistance, and ion adsorption at the electrode surface. When converting the diameter (Z' values) of the semicircles into ionic conductivities, the conductivity increased with increasing x , reached a maximum of 2.39 mS cm^{-1} at $x = 0.1$ (equivalent to 0.2 M AgCl), and then decreased (Figure 1B). The results indicate that the addition of 0.2 M AgCl significantly enhanced the conductivity of the AgCl-doped SE by more than 80% compared with the undoped LPS. Subsequent experiments and calculations on LPS and AgCl-doped LPS revealed that the electronic conductivity of LPS is further lowered after AgCl doping, suggesting that the AgCl-doped LPS can be a reliable SE with both ion-conducting and electron-insulating properties (see Additional notes in Supporting Information). This enhancement positions both undoped LPS and AgCl-doped LPS as promising materials for exploring the dopant effects and the corresponding diffusion mechanisms.

The repetition of the conductivity measurement at differing temperatures gives rise to the temperature dependence of ionic conductivity, which can be used to assess the activation energy for Li diffusion. To this end, we measured the impedance spectra for the synthesized samples ($\text{Li}_{7-2x}\text{P}_3\text{Ag}_x\text{S}_{11-x}\text{Cl}_x$ with $x = 0.0, 0.05, 0.1, 0.15,$

and 0.2) under differing temperatures in the range of 25–80°C and drew their temperature dependence using the Arrhenius plots (Figure 1C). Overall, the measured ionic conductivity follows the Arrhenius relation of $\sigma \propto \exp(-E_a/kT)$ except the slight deviation at $>50^\circ\text{C}$ of AgCl-doped LPS ($\text{Li}_{7-2x}\text{P}_3\text{Ag}_x\text{S}_{11-x}\text{Cl}_x$ with $x = 0.2, 0.3, 0.4$). Such a phenomenon has also been observed in some Li SEs with halide elements, where the SE samples undergo phase transitions into highly conductive phases at $>60^\circ\text{C}$ and exhibit higher ionic conductivity than the linear fitting lines.^{22,23} When evaluating the energy barriers (E_a) using the Arrhenius relation, the energy barriers of all AgCl-doped samples are lower than that (0.22 eV) of undoped LPS (Figure 1D). The lowest energy barrier was observed for the 0.2 M AgCl-doped LPS ($\text{Li}_{6.8}\text{P}_3\text{Ag}_{0.1}\text{S}_{10.9}\text{Cl}_{0.1}$) with a value of 0.17 eV (detailed data are in Table S1). The improved conductivity and reduced activation energy measured for the AgCl-doped LPS confirm that the minor addition of AgCl to the LPS indeed improved Li diffusion. Considering that the observed difference in the ionic conductivity is related to the difference in the structures of the SEs, precise identification of the atomic structures is necessary for understanding the mechanism underlying improved Li diffusion kinetics.

2.2 | Atomic-scale structure of the LPS SEs

To identify the atomic structures that are responsible for the ionic conductivity of SEs, we first identified the phases using X-ray diffraction (XRD) to construct the SE samples (Figure 2A). When examining the reference LPS and the counterpart sample of 0.2 M AgCl-doped LPS ($\text{Li}_{6.8}\text{P}_3\text{Ag}_{0.1}\text{S}_{10.9}\text{Cl}_{0.1}$), both samples were found to be glass ceramics with very high crystallinity (90% and 93% for the undoped and 0.2 M AgCl-doped LPS, respectively) (Figure S1). The major phase of the LPS is the triclinic $\text{Li}_7\text{P}_3\text{S}_{11}$ crystal belonging to a $(P\bar{1})$ space group (PDF 04-014-8383). Notably, the XRD spectra of the $\text{Li}_{6.8}\text{P}_3\text{Ag}_{0.1}\text{S}_{10.9}\text{Cl}_{0.1}$ were almost identical to those of the undoped LPS and did not show any peaks associated with secondary phases related to AgCl and residual raw materials. This suggests that complete solid-state reactions have taken place by appropriately substituting the host atom sites in the $\text{Li}_7\text{P}_3\text{S}_{11}$ phase with Ag and Cl atoms.

The question naturally arises as to why two SE samples with the same crystalline phase exhibit different

conductivities. To tackle this issue, it is necessary to resolve the atomic structures beyond the resolution limit of XRD. This is because the fundamental structural motifs, such as PS_4 and P_2S_7 (Figure 2B) comprising the $\text{Li}_7\text{P}_3\text{S}_{11}$ crystalline phase, may differ owing to differing dopant properties such as oxidation number and ionic radius. Raman spectroscopy was employed to further analyze the structural differences between undoped LPS and the 0.2 M AgCl-doped LPS (Figure 2C,D). Raman spectra of the LPS sample exhibited bands at 420 and 405 cm^{-1} , corresponding to the PS_4 and P_2S_7 clusters, respectively. However, for the 0.2 M AgCl-doped LPS, an additional band at 385 cm^{-1} with low intensity was observed in addition to the characteristic PS_4 and P_2S_7 bands. The X-ray photoelectron spectroscopy (XPS) observation of the 0.2 M AgCl-doped LPS confirmed the existence of a bond between P and Cl (Figure S2), indicating the creation of a new substructure by AgCl doping. Further structural analysis using Rietveld refinement and DFT revealed that the corner S atom of P_2S_7 was substituted by Cl, forming the di-tetrahedral $\text{P}_2\text{S}_6\text{Cl}$ as shown in the later section. Hence, the new 385 cm^{-1}

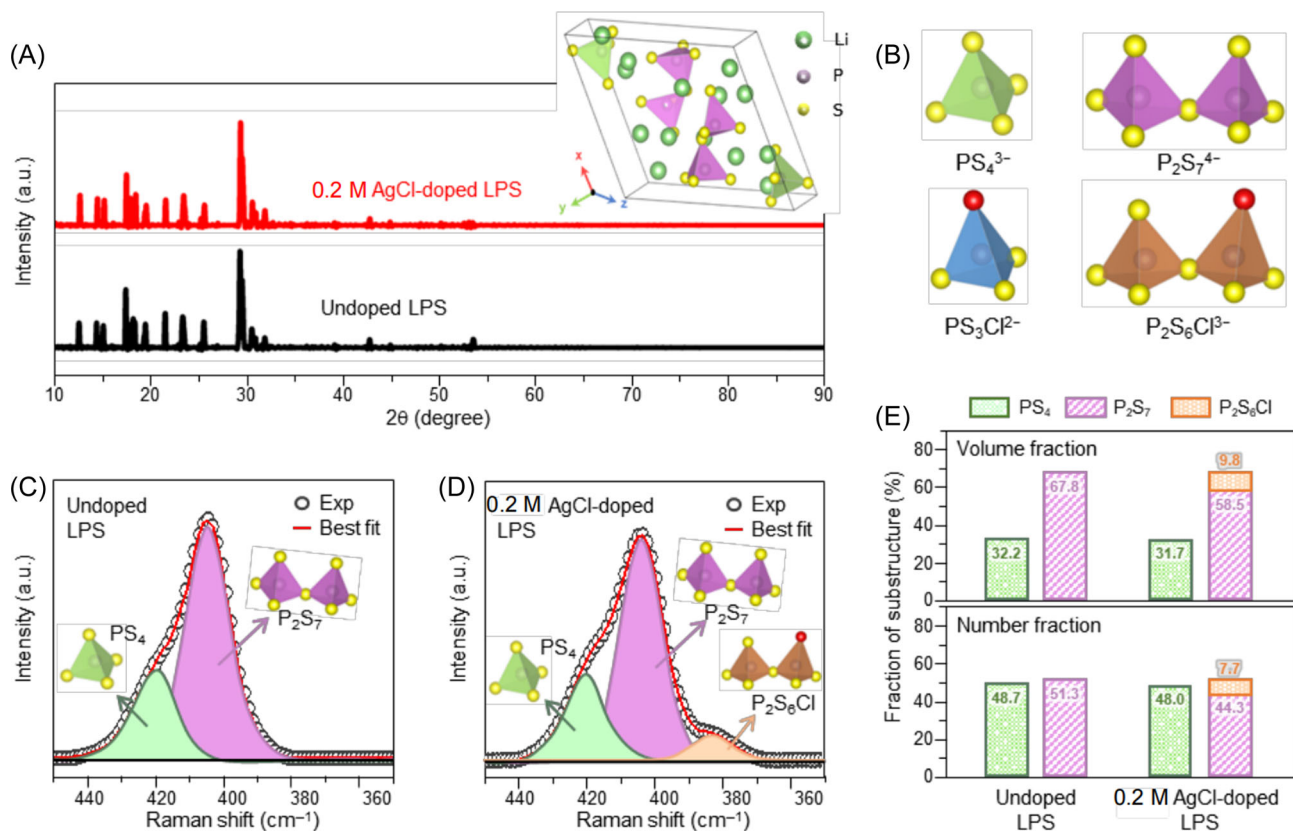


FIGURE 2 (A) XRD spectra of the undoped LPS and 0.2 M AgCl-doped LPS ($\text{Li}_{6.8}\text{P}_3\text{Ag}_{0.1}\text{S}_{10.9}\text{Cl}_{0.1}$). The inset in (A) is the standard crystal structure of the triclinic $\text{Li}_7\text{P}_3\text{S}_{11}$ crystal. (B) Schematics showing the configuration of the representative PS_x motifs comprising the undoped LPS. Characteristic Raman bands deconvoluted from the Raman spectra of the (C) undoped LPS and (D) 0.2 M AgCl-doped LPS SEs, indicating the presence of various PS_x motifs. (E) Number and volume fractions of the PS_4 and P_2S_7 -type motifs comprising the LPS and $\text{Li}_{6.8}\text{P}_3\text{Ag}_{0.1}\text{S}_{10.9}\text{Cl}_{0.1}$ SEs.

band observed in Figure 2C is assumed to correspond to P_2S_6Cl .

Subsequent Gaussian deconvolution of characteristic peaks revealed the number and volume fractions of PS_x motifs in the SEs (Figure 2E). For the undoped LPS, ditetrahedral P_2S_7 motifs occupy a twice larger volume than that of PS_4 , which renders the P_2S_7 motif the dominant structure that contributes to the shape of Li migration pathways and thus the ionic conductivity of SEs.¹⁰ Doping the LPS SE with AgCl results in a partial substitution of P_2S_7 by P_2S_6Cl . This can modify the Li migration pathways surrounded by P_2S_7 , subsequently altering the Li diffusion kinetics. Thus, to comprehend the impact of the AgCl dopant on ionic conductivity, it is crucial to accurately replicate the structures of the undoped LPS and 0.2 M AgCl-doped LPS.

2.3 | Replication of atomic-scale structures for simulations

To reconstruct the crystal structures of the SE samples before and after doping, we extracted atomic structures

using synchrotron Rietveld refinement analysis (see Methods and Tables S2 and S3 in the Supporting Information) and validated the resultant structures with DFT calculations (Figure 3). Figure 3A shows the fitting patterns and refinement parameters of the undoped LPS, exhibiting well-fitted results using a single-phase model of the $Li_7P_3S_{11}$ crystal, with a low R_{wp} value of 4.195. With the $P\bar{1}$ space group, the refined $Li_7P_3S_{11}$ crystal has 7, 3, and 11 symmetrically unique Li^+ , P^{5+} , and S^{2-} sites, respectively (Figure 3B). When doping with AgCl, the Ag^+ and Cl^- dopants preferentially replace the elements with similar oxidation states, leading to Ag^+ and Cl^- substitutions for Li^+ and S^{2-} , respectively. Upon the Cl^- substitution for S^{2-} , the charge difference in these anions induces the excess positive charge to the SE, which is readily compensated by the removal of mobile Li^+ ions (i.e., the formation of Li^+ vacancy).^{24,25} As a result, the LPS after AgCl doping has charge-balanced stoichiometry of $Li_{7-2x}P_3Ag_xS_{11-x}Cl_x$. To identify the preferential doping sites in LPS, the Rietveld refinement was carried out on the 0.2 M AgCl-doped LPS (Figure 3C). The Rietveld refinement was well fitted to the LPS crystal with an R_{wp} value of 4.460, indicating that the majority of

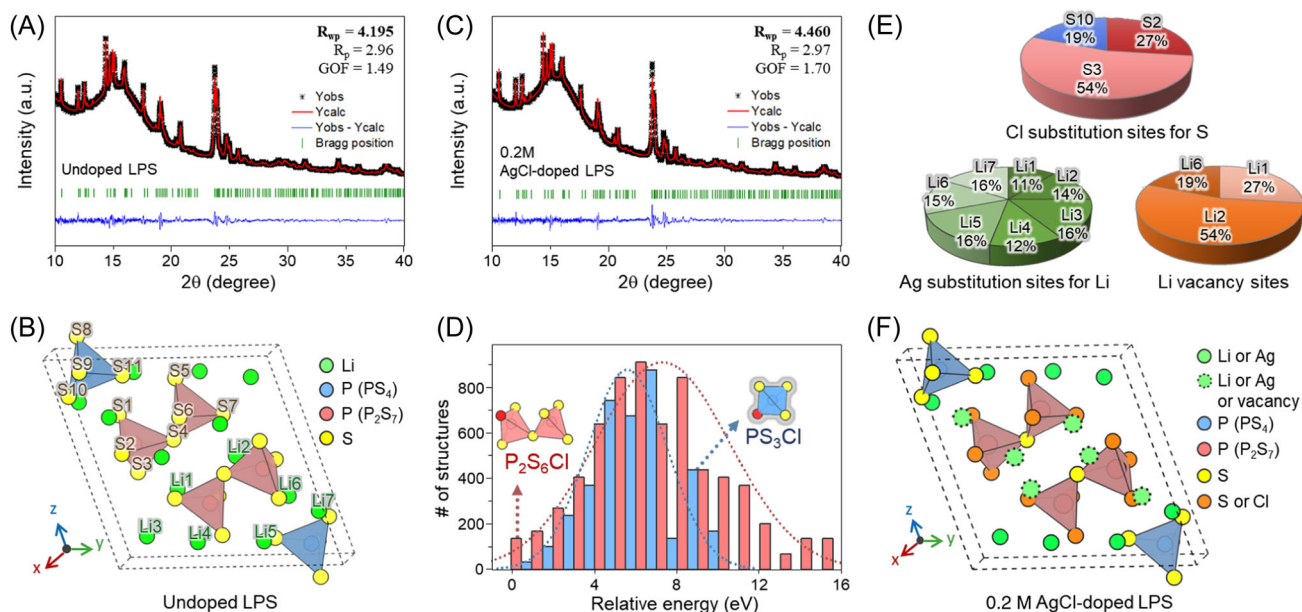


FIGURE 3 (A) Synchrotron X-ray spectra superimposed with Rietveld refinement pattern of the undoped LPS and (B) corresponding structure determined by synchrotron Rietveld analysis. Black stars—experimental data; red lines—fitted data; blue lines—difference between the observed and calculated data; green vertical lines—Bragg peak positions of $Li_7P_3S_{11}$. (C) Synchrotron X-ray spectra superimposed with Rietveld refinement patterns of the 0.2 M AgCl-doped LPS. The halo peaks at the low-angle side ($\sim 18^\circ$) of (A) and (C) correspond to the peak for the airtight X-ray sample holder. (D) Histogram of the electrostatic energies calculated for 8316 possible structures of $Li_{6.5}Ag_{0.25}P_3S_{10.75}Cl_{0.25}$ (i.e., 0.5 M AgCl-doped LPS) generated after enumerating possible positions of Ag and Cl dopants, and Li vacancy. The structures with P_2S_6Cl and PS_3Cl are denoted by red and blue bars, respectively. (E) Ratios of Ag and Cl dopants, and Li vacancy positions observed from the 100 stable $Li_{6.5}Ag_{0.25}P_3S_{10.75}Cl_{0.25}$ model structures. (F) 0.2 M AgCl-doped LPS structure determined by structure prediction and Synchrotron X-ray Rietveld analysis.

Ag and Cl atoms are embedded in the LPS SE. Further examination of Rietveld refinement, with specific Ag and Cl positions considered, revealed that Cl dopants are less likely to occupy the S4 site out of the 11 S-sites within the unit cell (see Figure S3). Also, the refined structure of 0.2 M AgCl-doped LPS showed that AgCl doping expands the crystal lattice of LPS, which further supports the incorporation of Ag ions into the crystal $\text{Li}_7\text{P}_3\text{S}_{11}$ phase (see Additional notes in Supporting Information).

Although the Rietveld analysis result is informative, it is challenging to reproduce the $\text{Li}_{7-2x}\text{P}_3\text{Ag}_x\text{S}_{11-x}\text{Cl}_x$ structure using DFT calculations considering all 10 potential Cl substitution sites because of the enormous numbers of crystal structures arising from the possible arrangements of Ag and Cl dopants, and Li vacancies. In particular, to construct a model crystal structure of 0.2 M AgCl-doped LPS ($\text{Li}_{6.8}\text{P}_3\text{Ag}_{0.1}\text{S}_{10.9}\text{Cl}_{0.1}$), supercells with the size of at least 209 atoms are necessary, leading to the 531,300 possible atomic arrangements. To reduce the computational cost while rapidly exploring preferential dopant and vacancy positions, we modeled more heavily doped LPS (0.5 M AgCl-doped LPS, $\text{Li}_{6.5}\text{P}_3\text{Ag}_{0.25}\text{S}_{10.75}\text{Cl}_{0.25}$) using 83-atom supercells. We then calculated electrostatic energies for all possible atomic arrangements of 8316 structures (see Methods in the Supporting Information) to screen out the unstable structures that hardly form in experiments (Figure 3D). The results show that all stable $\text{Li}_{6.5}\text{P}_3\text{Ag}_{0.25}\text{S}_{10.75}\text{Cl}_{0.25}$ structures with relative electrostatic energies lower than 1.0 eV commonly have di-tetrahedral $\text{P}_2\text{S}_6\text{Cl}$, rather than tetrahedral PS_3Cl , suggesting that Cl atoms are preferentially doped on P_2S_7 . Further analysis of the 100 stable $\text{Li}_{6.5}\text{P}_3\text{Ag}_{0.25}\text{S}_{10.75}\text{Cl}_{0.25}$ structures revealed that, for the majority (81%) of these structures, Cl occupies the corner S sites of S2 and S3 in P_2S_7 (Figure 3E). Subsequent Madelung potential calculations on S sites also confirmed that Cl is likely to replace S sites in S2 and S3 (see Figure S4). As Cl^- dopants are inserted into $(\text{P}_2\text{S}_7)^{4-}$ ionic clusters to create $(\text{P}_2\text{S}_6\text{Cl})^{3-}$, Li vacancy with a negative charge tends to form near di-tetrahedral $\text{P}_2\text{S}_6\text{Cl}$, which is evidenced by the preferential Li vacancy formation in Li1, Li2, and Li6 sites. Unlike Cl dopant and Li vacancy, Ag is found to have no preferential doping sites and can replace any Li sites in LPS.

The above findings on the preferential doping sites revealed that the introduced Cl atoms displayed a preference for specific sites, namely, those in the corner S of the P_2S_7 di-tetrahedra rather than the tetrahedral PS_4 motif, which led to the formation of $\text{P}_2\text{S}_6\text{Cl}$. The above results based on Rietveld analyses and DFT calculations further confirm the presence of a Raman peak at 385 cm^{-1} in the AgCl-doped LPS (Figure 2D). The specific Ag and Cl positions, together with the lattice parameters obtained from Rietveld refinement, allowed

the reconstruction of the atomic structure of the 0.2 M AgCl-doped LPS as shown in Figure 3F (see Tables S2 and S3 for the detailed atomic configurations).

2.4 | Li diffusion mechanisms and their doping response

The Li diffusion pathways in LPS-type SEs correspond to the spaces surrounded by the PS_x substructures/motifs, and thus the Li diffusion kinetics are affected by the distributions²⁶ and movements²⁷ of these substructures. For example, when the S atoms comprising PS_x substructures are arranged in a body-centered cubic structure (as seen in compounds like $\text{Li}_7\text{P}_3\text{S}_{11}$ and $\text{Li}_{10}\text{GeP}_2\text{S}_{12}$), the SEs tend to display flat energy landscapes for Li diffusions, resulting in high ionic conductivity compared with compounds with hexagonal close-packed anion sublattices (e.g., Li_3PS_4 and Li_4GeS_4).²⁶ In addition, a recent theory proposed that sulfide tetrahedral clusters (MS_4^{n-} , $n = 3$ or 4) can facilitate Li diffusion through their translational and rotational motions by binding with adjacent Li^+ ions.²⁷ This phenomenon is commonly referred to as the “paddle-wheel effect.” From these perspectives, the Li diffusion kinetics is strongly correlated with the movements of PS_x substructures, and thus, tracing their movements is key to understanding the ionic conductivity of LPS and AgCl-doped LPS. However, the previous studies describing the movement of PS_x substructures were constrained by the size of the atomic structures and simulation time, as they relied on first-principles calculations, which were limited to structures containing less than 100 atoms. One example of failure arising from such spatiotemporal limitations is the absence of hypo-thiophosphate $[(\text{P}_2\text{S}_6)^{4-}]$ and P_3S_{10} substructures in the model LPS structures, which were often observed in X-ray absorption spectroscopy (XAS) and XPS analyses of $x\text{Li}_2\text{S}-y\text{P}_2\text{S}_5$ glass ceramics.^{28–30}

ANN-based MD is a new simulation technique that can handle a large number (~2000) of atoms without limitations of pseudopotential, offering a more comprehensive understanding of the diffusion behavior with an accuracy comparable to first-principles molecular dynamics. With this technique, we find it feasible to accurately describe the movement of PS_x substructures and their effect on the Li diffusion kinetics.

2.4.1 | Transformation of various PS_x substructures

To track the movement and structural changes of various PS_x motifs during Li diffusion, we initially constructed a

model structure containing 1512 atoms, representing the undoped LPS (see Methods in the Supporting Information). Subsequent simulations based on ANN-based MD revealed Li diffusion pathways through the spaces encaged by the PS_4 and P_2S_7 di-tetrahedra (Figure 4A). Careful examinations revealed that some Li ions diffuse across di-tetrahedral P_2S_7 motifs, indicating that Li ions can penetrate through di-tetrahedral P_2S_7 motifs. Further analysis of the snapshots of MD simulations showed that P_2S_7 motifs disrupt/dissociate into PS_4 and PS_3 , opening new passages for Li ions. Subsequently, the dissociated PS_3 structures then attach to adjacent PS_4 tetrahedra to create another P_2S_7 di-tetrahedra through the reaction $PS_3 + PS_4 \rightarrow P_2S_7$ (see the inset of Figure 4A). This process maintains the overall number fraction of $PS_4:P_2S_7$ at an approximate 1:1 ratio, as shown in Figure 2E. This transformation ($PS_3 + PS_4 \rightarrow P_2S_7$) allows Li ions to diffuse through di-tetrahedral P_2S_7 motifs and diversifies the Li diffusion pathways, which can be a potential reason for the high ionic conductivity of LPS SEs.

To further investigate the effect of dopants in the structural transformation of PS_4 and P_2S_7 clusters, we next constructed large-scale 3D structures that can describe the effect of Ag and Cl dopants on LPS SEs. We separately analyzed the effect of each dopant on the

diffusion mechanism by constructing the model structures of SEs doped with only Ag (i.e., Ag-doped LPS, $Li_{6.75}Ag_{0.25}P_3S_{11}$) and with only Cl (i.e., Cl-doped LPS, $Li_{6.75}P_3S_{10.75}Cl_{0.25}$), which were done by high-throughput computational screening among all possible atomic configurations of dopants and Li vacancies (see Methods in the Supporting Information). The simulations on the Ag- and Cl-doped LPS displayed new structural transformations of PS_x motifs, which were not observed in the undoped LPS model structure. For Cl-doped LPS, P_2S_6Cl clusters undergo the breakage of P-Cl bonds and subsequent interaction with nearby PS_4 tetrahedra, leading to the formation of P_3S_{10} clusters according to the transformation $P_2S_6Cl + PS_4 \rightarrow P_3S_{10} + Cl$ (Figure 4B). Such structural transformation is attributed to the changes in the P:S ratio resulting from Cl doping: LPS-type SEs synthesized using Li_2S and P_2S_5 compounds can have various PS_x motifs depending on the P:S ratio. For example, for S-poor compounds, the most stable motif is P_3S_{10} , followed by P_2S_6 , P_2S_7 , and PS_4 .²⁸ From this perspective, the formation of P_3S_{10} arises from the reduced S composition due to Cl doping. On the other hand, Ag-doped LPS has relatively heavy Ag ions located between PS_4 and P_2S_7 , which inhibits the $PS_3 + PS_4 \rightarrow P_2S_7$ transformation observed in the undoped LPS. Instead, two

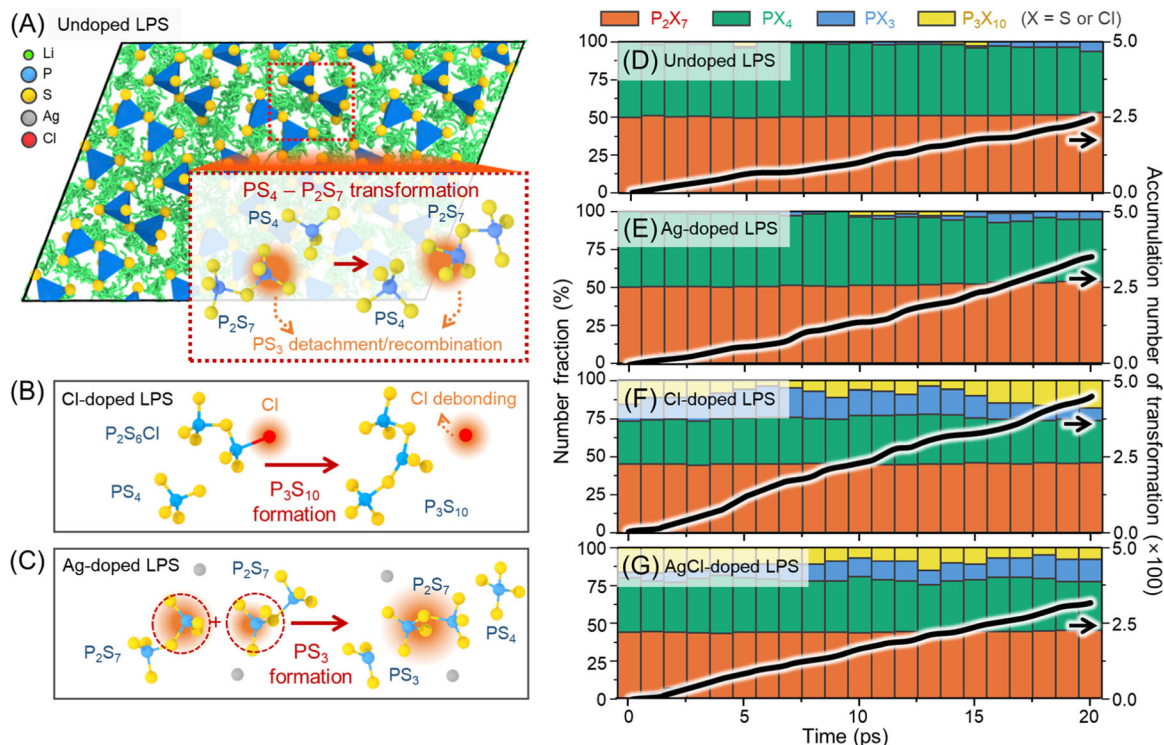


FIGURE 4 (A) Cross-section of a large-scale 3D structure used for ANN-based MD simulations, showing Li diffusion pathways (in green) in the LPS crystal at 400 K. Snapshots showing the structural transformation confirmed during MD calculations; $PS_4 \rightarrow P_2S_7$ in the LPS structure, (B) $PS_4 + P_2S_6Cl \rightarrow P_3S_{10} + Cl$ in Cl-doped LPS ($Li_{6.75}Ag_{0.25}P_3S_{11}$), and (C) $P_2S_7 + P_2S_7 \rightarrow PS_3 + PS_4 + P_2S_7$ in Ag-doped LPS ($Li_{6.75}Ag_{0.25}P_3S_{11}$). Changes in the number fraction of the substructures in (D) LPS, (E) Ag-doped LPS, and (F) Cl-doped LPS and (G) AgCl-doped LPS measured as a function of simulation time. The cumulative counts (black lines) of structure transformations are superimposed for comparison.

P_2S_7 di-tetrahedra in Ag-doped LPS can interact with each other to generate PS_3 and PS_4 (Figure 4C). The relatively unstable PS_3 clusters then combine with nearby PS_4 to create new P_2S_7 di-tetrahedra.

The above structural transformations were further confirmed by statistical analyses on the number fractions of PS_x clusters and the frequency of structural transformations (Figure 4D–F). In the case of LPS (Figure 4D), the frequency of structural transformations increases over time while the number fractions of PS_4 and P_2S_7 remain nearly the same, which suggests that the two types of clusters keep transforming to each other via $PS_3 + PS_4 \rightarrow P_2S_7$ transformation. In contrast, ANN-based MD simulations performed on the Ag-doped LPS showed that the number fraction of PS_3 clusters increases slightly with time (Figure 4E), which stems from the formation and accumulation of PS_3 clusters after the interaction between two P_2S_7 clusters (Figure 4C). Compared with the undoped LPS and Ag-doped LPS model structures, the frequency of structure transformations is greater for the Cl-doped LPS (Figure 4F), which may be because of the P_3S_{10} clusters that can readily react with adjacent PS_4 tetrahedra according to the formula $P_3S_{10} + PS_4 \rightarrow PS_4 + P_3S_{10}$. The number fraction of the thus-formed P_3S_{10} motifs fluctuates during MD simulations, which is attributed to the various intermediate structures generated during the dissociation and bonding of P–S bonds. For instance, the P_3S_{10} formed in Cl-doped LPS can undergo the following subsequent structure transformations: $P_3S_{10} + PS_4 \rightarrow P_2S_7 + PS_3 + PS_4 \rightarrow P_2S_7 + P_2S_7 \rightarrow PS_4 + PS_3 + P_2S_7 \rightarrow PS_4 + P_3S_{10}$. Such transformations occur over 0.5–10 ps of simulation time. As a result, depending on the simulation time when counting the number of structural motifs, the quantity of P_3S_{10} may appear to increase or decrease over time. When both Ag and Cl dopants are introduced into LPS (Figure 4G), the influences of two dopants are combined: Cl dopants create P_3S_{10} motifs through the reaction $P_2S_6Cl + PS_4 \rightarrow P_3S_{10} + Cl$ (Figure 4B), whereas Ag dopants increase the number fraction of PS_3 motifs via the reaction $2P_2S_7 \rightarrow P_2S_7 + PS_3 + PS_4$ (Figure 4C). Various structural transformations of PS_x motifs displayed from the LPS SEs can alter energy landscapes for Li diffusions, which can facilitate the fast migration of Li^+ ions from one site to another.

2.4.2 | Paddle-wheel dynamics

In recent times, paddle-wheel dynamics has emerged as a mechanism for elucidating superionic conductivity. This concept proposes that anion clusters, formed by multiple atoms bound through covalent bonds (e.g., SO_4^{2-} , NO_2^- ,

PS_4^{3-} , and PO_4^{3-}), electrostatically adhere to cations and undergo rotation, thereby facilitating cation mobility.^{31–34} Depending on the configurations of the anion clusters, certain clusters (e.g., P_2S_7) can demonstrate not only rotational but also translational movement, thereby further amplifying the mobility of adjacent Li ions.¹⁷ From this perspective, the PS_x clusters [i.e., $(PS_4)^{3-}$, $(P_2S_7)^{4-}$, $(P_3S_{10})^{5-}$, $(PS_3)^{-}$] observed in Figure 4 can also undergo unique rotational/translational motions to improve the ionic conductivity of SEs. Figure 5A shows the representative motions of the four different PS_x clusters (i.e., PS_4 , P_2S_7 , P_3S_{10} , PS_3) observed in the Ag- and Cl-doped LPS model structures, where all types of motions commonly show the angular displacements of P–S bonds. This suggests that the angular displacements can serve as a quantitative parameter to assess the extent of the paddle-wheel effect in Ag- and Cl-doped LPS. This assessment was conducted in the study by calculating the mean angular displacements ($\langle\theta\rangle$) of P–S bonds in PS_x clusters of model SE structures (see Methods in the Supporting Information).

When analyzing PS_x clusters in undoped LPS (Figure 5B), it becomes clear that P_2S_7 exhibits more prominent paddle-wheel motion in comparison to PS_4 , as supported by the larger $\langle\theta\rangle$ observed for P_2S_7 . This is primarily attributed to the greater degree of freedom of P_2S_7 with bending and twisting motions, which are not feasible in PS_4 (Figure 5A). On the other hand, PS_3 motifs in Ag-doped LPS exhibit a distinctive rotational behavior: over time, the $\langle\theta\rangle$ values show an average value of 29.90° and a standard deviation of 8.28° (Figure 5C). The large standard deviation and associated fluctuation in $\langle\theta\rangle$ values are attributed to the statistical error arising from the small number fraction (0.0%–6.3%) of PS_3 motifs in Ag-doped LPS (Figure 4E). On the other hand, the large time-averaged $\langle\theta\rangle$ value indicates the readily rotatable feature of PS_3 motifs. This is attributed to the tendency of PS_3 motifs to rapidly rotate and combine with nearby PS_4 motifs (Figure 5A). The other cluster, P_3S_{10} , is mostly generated for Cl-doped LPS (Figure 4F) and exhibits a large degree of rotational motion owing to the bending and stretching motions of two P–S–P bonds (Figure 5A). Overall, the paddle-wheel dynamics is the most active for the PS_3 cluster, followed by P_3S_{10} , P_2S_7 , and PS_4 . This trend is also observed for AgCl-doped LPS ($Li_{6.5}Ag_{0.25}P_3S_{10.75}Cl_{0.25}$) model structures (see Figure 5E). The above results demonstrate that both Ag and Cl dopants enhance the paddle-wheel motion by generating readily rotatable and flexible PS_3 and P_3S_{10} motifs. The dynamic movements of these motifs can improve the Li diffusion kinetics in SEs, resulting in the high ionic conductivity observed in AgCl-doped LPS, as shown in Figure 1.

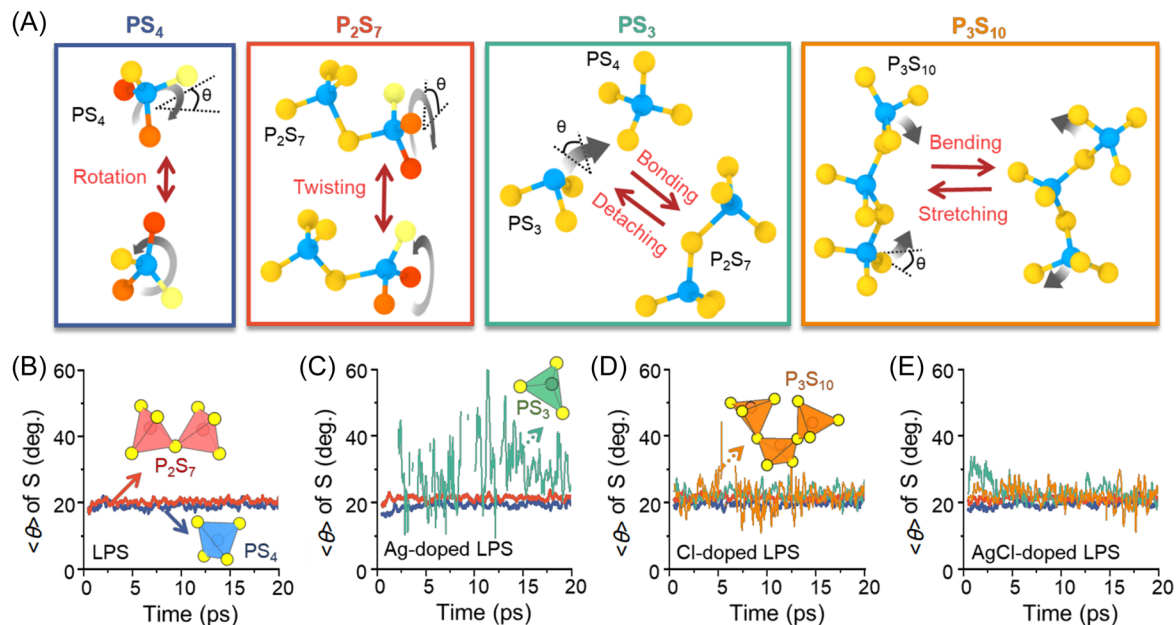


FIGURE 5 (A) Representative motions of PS_x motifs observed from the undoped LPS, Ag-doped, and Cl-doped LPS model structures. Each motion may lead to the angular displacements of P-S bonds as quantified by $\langle \theta \rangle$. Mean angular displacements $\langle \theta \rangle$ of P-S bonds in PS_x motifs of the (B) undoped LPS, (C) Ag-doped, (D) Cl-doped, and (E) AgCl-doped LPS model structures.

2.5 | Effect of diffusion mechanisms on the ionic conductivity

2.5.1 | Quantification of diffusion kinetics

Based on the above findings, it is concluded that the high ionic conductivity of AgCl-doped LPS arises from the combination of two mechanisms: (1) structure transformations in PS_x motifs through the creation of new Li-ion passages (Figure 4) and (2) amplified paddle-wheel motion of PS_x motifs through Ag and Cl doping (Figure 5). To analyze the effect of these diffusion mechanisms on the ionic conductivity of AgCl-doped LPS, we quantified the degree of each mechanism in the model structures. This was achieved by estimating the time average of $\langle \theta \rangle$ values, ($\langle \tilde{\theta} \rangle$) and the total number of structure transformations, (N_{trans}) of PS_x motifs during simulations (Table 1). Comparison of the $\langle \tilde{\theta} \rangle$ and N_{trans} values revealed that the LPS structures doped with Ag and Cl always exhibit higher values than those of the undoped LPS at all temperature ranges, indicating that AgCl doping is an effective method for improving both structure transformations in PS_x motifs and paddle-wheel dynamics.

2.5.2 | Interpretation of the improved ionic conductivity

To quantitatively compare how each diffusion mechanism influences the ionic conductivity of LPS SEs, we

evaluated the Li-ion diffusivity (D_{Li}) as a representative parameter of the ionic conductivity. To remove the errors arising from the random distribution of atomic velocities, molecular dynamic simulations were repeated six times for each model structure and the average D_{Li} values were used for estimating the energy barriers (see Methods and Figure S5 in the Supporting Information). Figure 6A,B illustrates the Arrhenius plot of the diffusivities calculated for the LPS SEs before and after doping with Ag and Cl. In the case of the undoped LPS (Figure 6A), the energy barrier for Li diffusion is relatively higher (0.085 eV) compared with those (0.079–0.083) evaluated for Ag-, Cl-, and AgCl-doped LPS. This high energy barrier mainly arises from that the PS_x motifs in LPS hardly undergo transformation into other structures, leading to the limited paddle-wheel effects with relatively less rotatable PS₄ and P₂S₇ motifs (see Table 1). This result indicates that the Li diffusion through the PS_x motifs becomes difficult in the undoped LPS owing to the suppression of PS_x transformations, leading to a relatively lower ionic conductivity than AgCl-doped LPS counterparts. In contrast to the undoped LPS, the Ag-, Cl-, and AgCl-doped LPS consistently demonstrated higher Li diffusivity compared with undoped LPS (Figure 6A): the D_{Li} of AgCl-doped LPS (Li_{6.5}Ag_{0.25}P₃S_{10.75}Cl_{0.25}) is greater by 28% compared with that of pristine LPS. The increase rate of Li diffusivity is consistent with that of the measured ionic conductivity, where the ionic conductivity of 0.4 M AgCl-doped LPS (Li_{6.6}Ag_{0.2}P₃S_{10.8}Cl_{0.2})

TABLE 1 Total number of transformations between PS_x motifs (N_{trans}), time average of $\langle\tilde{\theta}\rangle$ of P–S bonds ($\langle\tilde{\theta}\rangle$), Li diffusivity (D_{Li}) calculated for LPS, Ag-doped LPS ($\text{Li}_{6.75}\text{Ag}_{0.25}\text{P}_3\text{S}_{11}$), Cl-doped LPS ($\text{Li}_{6.75}\text{P}_3\text{S}_{10.75}\text{Cl}_{0.25}$), AgCl-doped LPS ($\text{Li}_{6.5}\text{Ag}_{0.25}\text{P}_3\text{S}_{10.75}\text{Cl}_{0.25}$) at different temperatures.

	Temp (K)	N_{trans}	$\langle\tilde{\theta}\rangle$ (°)	D_{Li} (cm^2/s)
LPS	300	31	16.9	2.35×10^{-5}
	350	109	18.4	3.53×10^{-5}
	400	246	19.5	4.81×10^{-5}
	450	583	21.1	6.48×10^{-5}
	500	663	21.9	7.50×10^{-5}
Cl-doped LPS	300	133	17.6	2.76×10^{-5}
	350	241	19.5	4.15×10^{-5}
	400	451	20.7	5.51×10^{-5}
	450	727	22.2	8.39×10^{-5}
	500	928	23.7	1.00×10^{-4}
Ag-doped LPS	300	37	17.0	2.85×10^{-5}
	350	164	18.5	4.04×10^{-5}
	400	352	20.1	6.94×10^{-5}
	450	592	21.1	8.24×10^{-5}
	500	885	22.7	9.55×10^{-5}
AgCl-doped LPS	300	79	17.5	2.67×10^{-5}
	350	244	19.1	4.11×10^{-5}
	400	318	20.8	6.97×10^{-5}
	450	671	22.0	7.06×10^{-5}
	500	884	23.5	9.71×10^{-5}

showed 37% improvement over that of LPS (see Additional notes in Supporting Information). This enhancement is attributed to the amplified paddle-wheel motion associated with the formation of PS_3 and P_3S_{10} motifs (see Figure 5 and Table 1), the behavior of which was also confirmed by the subsequent calculations on the number fractions of PS_x motifs at various temperatures (see Figures S6–S7). The above results also suggest that, regardless of the weight or size of dopants (e.g., Ag being heavier than Li, Cl being lighter than S), doping elements can promote the Li diffusion as long as they can enhance the structural changes and rotational degree of PS_x motifs (see Additional notes in Supporting Information for the detailed discussions).

When comparing the predicted and measured energy barriers, the calculated ones (0.079–0.085 eV) of LPS and AgCl-doped LPS in this study exhibit relatively lower values compared with the experimentally measured ones (0.17–0.22 eV). This is because, unlike atomic simulations that assume a defect-free

pure SE, the actual SE samples contain various defects that hinder Li-ion diffusions, such as grain boundaries, impurities, and precipitate phases. One of the main reasons that hinder Li diffusion is the limited doping capability of LPS: in general, a dopant atom can easily substitute the existing atom when (1) the ionic radius of the dopant is smaller than that of the host ion and (2) the dopant type (p- or n-type) matches that of the host semiconductor.³⁶ Considering that Li sulfide SE is close to an n-type semiconductor,³⁷ Cl^- , an n-type dopant with a small ionic radius compared with S^{2-} , can be readily incorporated into LPS. On the other hand, Ag^+ , with a larger radius compared with Li^+ , is more challenging to substitute for Li^+ . From this perspective, in experimentally synthesized samples, some Ag^+ may not have been effectively doped, leading to a potentially larger diffusion barrier than those predicted in LPS with complete AgCl dual doping.

2.5.3 | Design guidelines for LPS SEs with high ionic conductivity

Referring back to Table 1, it is evident that N_{trans} of PS_x motifs and time-averaged $\langle\tilde{\theta}\rangle$ exhibit a clearly proportional relationship with D_{Li} . If this relationship holds for other SE materials, one can use these two values (i.e., N_{trans} and $\langle\tilde{\theta}\rangle$) as the generic parameters for predicting the ionic conductivity of SEs. To validate this claim, we constructed the model structures for AgBr-, Br-, AgI-, and I-doped LPS and calculated N_{trans} of PS_x motifs, $\langle\tilde{\theta}\rangle$, and D_{Li} (see Methods in the Supporting Information). Comparison between these three parameters showed that both N_{trans} and $\langle\tilde{\theta}\rangle$ values exhibit clear linear relationships to the D_{Li} regardless of dopant types (Figure 6B). This suggests that both N_{trans} and $\langle\tilde{\theta}\rangle$ values can be used as the quantitative parameters for predicting the ionic conductivity of SEs. Specifically, N_{trans} and $\langle\tilde{\theta}\rangle$ values, representing the degree of the PS_x structure transformation and paddle-wheel dynamics, respectively, are proportional to D_{Li} following $D_{\text{Li}} = 7.9 \times 10^{-8}N_{\text{trans}} + 2.4 \times 10^{-5}$ and $D_{\text{Li}} = 1.1 \times 10^{-5}\langle\tilde{\theta}\rangle - 1.7 \times 10^{-4}$.

Based on the above findings, fully exploiting the rotational degrees of freedom (i.e., angular displacements of P–S bonds) and utilizing the paddle-wheel effect could be a viable way to develop Li-ion conductors with superior ionic conductivity. To grasp an insight into this idea, we calculated $\langle\tilde{\theta}\rangle$ values of various PS_x clusters for LPS with three different types of dopants, that is, AgCl, AgBr, and AgI (see Additional notes in Supporting Information for further discussions on the diffusivity of AgCl-, AgBr-, and AgI-doped LPS). Figure 6C shows that PS_3 and P_3S_{10} clusters exhibit a high degree of rotational

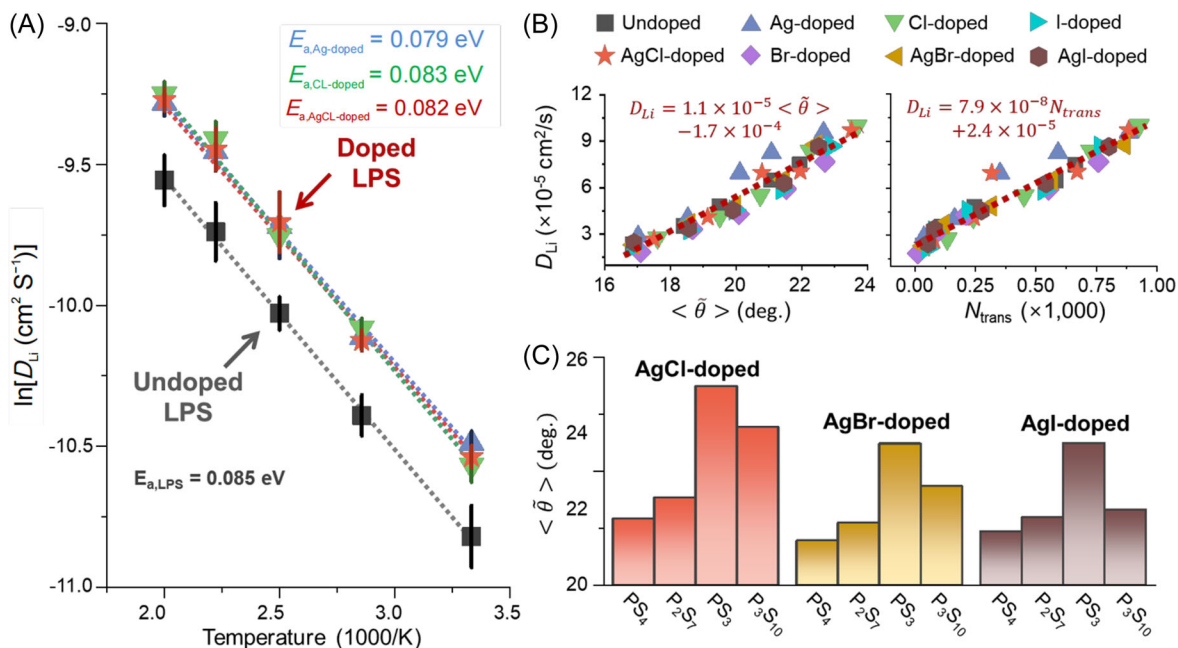


FIGURE 6 (A) Arrhenius diffusivity plots of LPS before and after doping, as predicted by ANN-based MD simulations. Standard deviation of the calculated diffusivities is denoted by vertical lines on the symbols, whereas the possible diffusivity values with a 90% credible interval are indicated as shaded areas. Diffusion mechanisms influencing D_{Li} are highlighted on the graphs for comparison. (B) D_{Li} of various model SE structures plotted over time-averaged $\langle \tilde{\theta} \rangle$ ($\langle \tilde{\theta} \rangle$) and the total number of structure transformations (N_{trans}) showing the linear relationships regardless of dopant types. (C) Comparison of $\langle \tilde{\theta} \rangle$ values calculated for various PS_x motifs in the AgCl-, AgBr-, and AgI-doped LPS model structures. D_{Li} values and associated Arrhenius plots were plotted using the post-processing software KINISI.³⁵

motions among all PS_x clusters, increasing the overall $\langle \tilde{\theta} \rangle$ values of LPS SEs. From this perspective, increasing the structure fraction of PS₃ and P₃S₁₀ clusters in LPS SEs can be an effective way to exploit the paddle-wheel mechanism for the design of superionic conductors. This can be achieved by destabilizing the P₂S₇ di-tetrahedra and facilitating the decomposition reaction of P₂S₇ → PS₃ + PS₄. Two experimentally feasible methods are (1) increasing the P₂S₅ portion of the Li₂S: P₂S₅ ratio during the synthesis procedure and (2) doping other elements to generate unstable P_{2-x}MS_{7-y}X (M and X represent cation and anion dopants, respectively) clusters. Therefore, we expect that this concept can be extended to developing future sulfide SEs with high ionic conductivity.

3 | CONCLUSION

Through a systematic study of the synthesis, electrochemical characterization and the atomic interpretation, we elucidated the role of Ag/Cl dual dopants on the superionic conduction of LPS SEs. The 0.2 M AgCl-doped LPS (Li_{6.8}P₃Ag_{0.1}S_{10.9}Cl_{0.1}) exhibited an ionic conductivity of 2.39 mS cm⁻¹, which is higher than that of undoped LPS (Li₇P₃S₁₁) by >80%. The atomic structures responsible for the high ionic conductivity of the 0.2 M

AgCl-doped LPS were reconstructed using combined techniques of synchrotron Rietveld analyses and atomic simulations. The Li-ion conductions in the refined atomic structures of the undoped LPS and AgCl-doped LPS were interpreted using large-scale ANN-based MD simulations. The subsequent statistical analysis successfully identified two key mechanisms governing the Li-ion conduction in the LPS SEs: (1) the structural transformations between PS_x clusters and (2) the correlational paddle-wheel dynamics.

We observed that the PS₄ and P₂S₇ motifs in the LPS transform from one to another by the dissociation/bonding of P-S bonds, allowing diverse Li diffusion pathways to penetrate through P₂S₇ motifs. The structural transformations of PS_x clusters can be modified and enhanced by doping with Ag and Cl: Ag promotes the interaction between two P₂S₇ di-tetrahedra, whereas Cl facilitates the breakage of P-Cl bonds of P₂S₆Cl, resulting in the formation of PS₃ and P₃S₁₀ as byproducts. Such diverse structure transformations open new pathways for Li-ion hopping, providing a favorable environment for Li diffusion. Second, unlike the classical paddle-wheel effect that focused primarily on the movements of pre-existing clusters (e.g., PS₄ and P₂S₇ clusters of LPS), the current study showed a more complete picture of paddle-wheel motions with the dynamic correlation between the

PS_x ionic clusters and Li-ions. Along with the PS_x transformations and formation of various PS_x clusters, paddle-wheel motions can be greatly enhanced. In particular, the readily rotatable/mobile PS₃ and P₃S₁₀ motifs generated by Ag or Cl doping enhance cation mobility at low temperatures by fostering paddle-wheel dynamics and thus facilitate the fast Li-ion conduction.

Based on the above findings, we identified two quantitative parameters that can be generically applied to predict the ionic conductivity of various SEs: N_{trans} , which quantifies the extent of the PS_x transformations, and $\langle \tilde{\theta} \rangle$, which measures the activity of paddle-wheel motions. In summary, the interconnected dynamics of the PS_x transformation and paddle-wheel effect elucidate the superionic conduction observed in the AgCl dual-doped LPSs. Based on this understanding, we propose strategies to amplify PS_x transformations and paddle-wheel mechanisms, potentially paving the way for the discovery of new superionic conductors.

4 | EXPERIMENTAL SECTION

The detailed procedures of synthesis, characterization, and atomic simulations that support the findings of this study are available in methods in Supporting Information of this article.

ACKNOWLEDGMENTS

J.-C. L. is grateful for the financial support from the National Research Foundation of Korea (NRF) grant funded by the Korean government (MEST, NRF-2021R1A2C2009596). Y.-S. C. also acknowledges research support from the NRF grant funded by the Korean government (Ministry of Science and ICT, MSIT) (No. RS-2023-00236572). We are also grateful to the UK Materials and Molecular Modelling Hub (MMM Hub), which is partially funded by the EPSRC (EP/P020194, EP/T022213), for computational resources on the Thomas and Young supercomputers, and to UCL for access to the Myriad (Myriad@UCL). Via our UK HEC Materials Chemistry Consortium membership, funded by the UK Engineering and Physical Sciences Research Council (EP/R029431), this work used the ARCHER2 UK National Super-computing Service (<https://www.archer2.ac.uk>). D. O. S. acknowledges support from the European Research Council, ERC (grant no. 758345). The Department of Materials Science and Engineering was supported through the Research-Focused Department Promotion & Interdisciplinary Convergence Research Project as a part of the Support Program for University Development for Dankook University in 2023. The authors also appreciate

technical support from Mr. Seong Kyun Park of Bruker AXS Korea.

CONFLICT OF INTEREST STATEMENT

The authors declare that there are no conflicts of interests.

DATA AVAILABILITY STATEMENT

Data will be made available on request.

ORCID

Kyung Yoon Chung  <http://orcid.org/0000-0002-1273-746X>

Jae-Chul Lee  <http://orcid.org/0000-0002-9294-2163>

REFERENCES

- Chen S, Xie D, Liu G, et al. Sulfide solid electrolytes for all-solid-state lithium batteries: structure, conductivity, stability and application. *Energy Storage Mater.* 2018;14:58-74.
- Lau J, DeBlock RH, Butts DM, Ashby DS, Choi CS, Dunn BS. Sulfide solid electrolytes for lithium battery applications. *Adv Energy Mater.* 2018;8(27):1800933.
- Wang Z, Jiang Y, Wu J, et al. Doping effects of metal cation on sulfide solid electrolyte/lithium metal interface. *Nano Energy.* 2021;84:105906.
- Song R, Xu R, Wang Z, et al. Oxide doping improving interface performance for Li₇P₃S₁₁ solid electrolytes. *J Alloys Compd.* 2022;921:166125.
- Kato Y, Hori S, Saito T, et al. High-power all-solid-state batteries using sulfide superionic conductors. *Nat Energy.* 2016;1(4):16030.
- Xu R, Xia X, Li S, Zhang S, Wang X, Tu J. All-solid-state lithium-sulfur batteries based on a newly designed Li₇P_{2.9}Mn_{0.1}S_{10.7}I_{0.3} superionic conductor. *J Mater Chem A.* 2017;5(13):6310-6317.
- Taklu BW, Su WN, Nikodimos Y, et al. Dual CuCl doped argyrodite superconductor to boost the interfacial compatibility and air stability for all solid-state lithium metal batteries. *Nano Energy.* 2021;90:106542.
- Rajagopal R, Ryu KS. Structural investigations, visualization, and electrolyte properties of silver halide-doped Li₇P₃S₁₁ lithium superionic conductors. *ACS Sustainable Chem Eng.* 2021;9(3):1105-1117.
- Zhang N, Ding F, Yu S, et al. Novel research approach combined with dielectric spectrum testing for dual-doped Li₇P₃S₁₁ glass-ceramic electrolytes. *ACS Appl Mater Interfaces.* 2019;11(31):27897-27905.
- Lee Y, Kim YH, An JH, Lee JC. Ionic conduction mechanisms in 70Li₂S-30P₂S₅ type electrolytes: experimental and atomic simulation studies. *Acta Mater.* 2022;235:118106.
- Liu Z, Fu W, Payzant EA, et al. Anomalous high ionic conductivity of nanoporous β-Li₃PS₄. *J Am Chem Soc.* 2013;135(3):975-978.
- Seino Y, Ota T, Takada K, Hayashi A, Tatsumisago M. A sulphide lithium super ion conductor is superior to liquid ion conductors for use in rechargeable batteries. *Energy Environ Sci.* 2014;7(2):627-631.

13. Heiranian M, DuChanois RM, Ritt CL, Violet C, Elimelech M. Molecular simulations to elucidate transport phenomena in polymeric membranes. *Environ Sci Technol*. 2022;56(6):3313-3323.
14. Sivaraman G, Guo J, Ward L, et al. Automated development of molten salt machine learning potentials: application to LiCl. *J Phys Chem Lett*. 2021;12(17):4278-4285.
15. Minami K, Hayashi A, Ujiie S, Tatsumisago M. Structure and properties of $\text{Li}_2\text{S}-\text{P}_2\text{S}_5-\text{P}_2\text{S}_3$ glass and glass-ceramic electrolytes. *J Power Sources*. 2009;189(1):651-654.
16. Mizuno F, Hayashi A, Tadanaga K, Tatsumisago M. High lithium ion conducting glass-ceramics in the system $\text{Li}_2\text{S}-\text{P}_2\text{S}_5$. *Solid State Ionics*. 2006;177(26-32):2721-2725.
17. Chang D, Oh K, Kim SJ, Kang K. Super-ionic conduction in solid-state $\text{Li}_7\text{P}_3\text{S}_{11}$ -type sulfide electrolytes. *Chem Mater*. 2018;30(24):8764-8770.
18. Fang H, Jena P. Argyrodite-type advanced lithium conductors and transport mechanisms beyond paddle-wheel effect. *Nat Commun*. 2022;13(1):2078.
19. Jansen M. Volume effect or paddle-wheel mechanism—fast alkali-metal ionic conduction in solids with rotationally disordered complex anions. *Angew Chem Int Ed*. 1991;30(12):1547-1558.
20. He X, Zhu Y, Mo Y. Origin of fast ion diffusion in super-ionic conductors. *Nat Commun*. 2017;8(1):15893.
21. Fu ZH, Chen X, Yao N, et al. The chemical origin of temperature-dependent lithium-ion concerted diffusion in sulfide solid electrolyte $\text{Li}_{10}\text{GeP}_2\text{S}_{12}$. *J Energy Chem*. 2022;70:59-66.
22. Zhang J, Li L, Zheng C, et al. Silicon-doped argyrodite solid electrolyte $\text{Li}_6\text{PS}_5\text{I}$ with improved ionic conductivity and interfacial compatibility for high-performance all-solid-state lithium batteries. *ACS Appl Mater Interfaces*. 2020;12(37):41538-41545.
23. Wei X, Shriver DF. High ionic conductivity in some lithium halide systems. *Chem Mater*. 2000;12(9):2528-2529.
24. Liu H, Yang Z, Wang Q, Wang X, Shi X. Atomistic insights into the screening and role of oxygen in enhancing the Li^+ conductivity of $\text{Li}_7\text{P}_3\text{S}_{11-x}\text{O}_x$ solid-state electrolytes. *Phys Chem Chem Phys*. 2019;21(48):26358-26367.
25. Deng Z, Radhakrishnan B, Ong SP. Rational composition optimization of the lithium-rich $\text{Li}_3\text{OCl}_{1-x}\text{Br}_x$ anti-perovskite superionic conductors. *Chem Mater*. 2015;27(10):3749-3755.
26. Wang Y, Richards WD, Ong SP, et al. Design principles for solid-state lithium superionic conductors. *Nat Mater*. 2015;14(10):1026-1031.
27. Zhang Z, Nazar LF. Exploiting the paddle-wheel mechanism for the design of fast ion conductors. *Nat Rev Mater*. 2022;7(5):389-405.
28. Dietrich C, Koerver R, Gaultois MW, et al. Spectroscopic characterization of lithium thiophosphates by XPS and XAS—a model to help monitor interfacial reactions in all-solid-state batteries. *Phys Chem Chem Phys*. 2018;20(30):20088-20095.
29. Garcia-Mendez R, Smith JG, Neuefeind JC, Siegel DJ, Sakamoto J. Correlating macro and atomic structure with elastic properties and ionic transport of glassy $\text{Li}_2\text{S}-\text{P}_2\text{S}_5$ (LPS) solid electrolyte for solid-state Li metal batteries. *Adv Energy Mater*. 2020;10(19):2000335.
30. Dietrich C, Weber DA, Sedlmaier SJ, et al. Lithium ion conductivity in $\text{Li}_2\text{S}-\text{P}_2\text{S}_5$ glasses—building units and local structure evolution during the crystallization of superionic conductors Li_3PS_4 , $\text{Li}_7\text{P}_3\text{S}_{11}$ and $\text{Li}_4\text{P}_2\text{S}_7$. *J Mater Chem A*. 2017;5(34):18111-18119.
31. Smith JG, Siegel DJ. Low-temperature paddlewheel effect in glassy solid electrolytes. *Nat Commun*. 2020;11(1):1483.
32. Zhang Z, Li H, Kaup K, Zhou L, Roy PN, Nazar LF. Targeting superionic conductivity by turning on anion rotation at room temperature in fast ion conductors. *Matter*. 2020;2(6):1667-1684.
33. Tang WS, Matsuo M, Wu H, et al. Liquid-like ionic conduction in solid lithium and sodium monocarbo-closo-decaborates near or at room temperature. *Adv Energy Mater*. 2016;6(8):1502237.
34. Tang WS, Unemoto A, Zhou W, et al. Unparalleled lithium and sodium superionic conduction in solid electrolytes with large monovalent cage-like anions. *Energy Environ Sci*. 2015;8(12):3637-3645.
35. McCluskey AR, Coles SW, Morgan BJ. Accurate estimation of diffusion coefficients and their uncertainties from computer simulation. *arXiv preprint*. 2023;2305(18244):1.
36. Williamson BAD, Buckeridge J, Chadwick NP, et al. Dispelling the myth of passivated codoping in TiO_2 . *Chem Mater*. 2019;31(7):2577-2589.
37. Gorai P, Famprikis T, Singh B, Stevanović V, Canepa P. Devil is in the defects: electronic conductivity in solid electrolytes. *Chem Mater*. 2021;33(18):7484-7498.

SUPPORTING INFORMATION

Additional supporting information can be found online in the Supporting Information section at the end of this article.

How to cite this article: Choi Y-S, Lee Y, Ahn H, et al. Exploring dopant-enhanced ionic conductivity of AgCl-doped $\text{Li}_7\text{P}_3\text{S}_{11}$ solid electrolytes: Integrating synchrotron Rietveld analysis, DFT, and ANN-based molecular dynamics approaches. *Carbon Energy*. 2024;e564. doi:10.1002/cey2.564